


Article

# Mathematical Modeling of the Floating Sleeper Phenomenon Supported by Field Measurements

Mojmir Uranjek<sup>1,2</sup>, Denis Imamović<sup>2</sup> and Iztok Peruš<sup>2,\*</sup> <sup>1</sup> Building and Civil Engineering Institute, Dimičeva 12, SI-1000 Ljubljana, Slovenia; mojmir.uranjek@um.si<sup>2</sup> Faculty of Civil Engineering, Architecture and Transportation Engineering, University of Maribor, Smetanova 17, SI-2000 Maribor, Slovenia; denis.imamovic@um.si

\* Correspondence: iztok.perus@um.si

**Abstract:** This article aims to provide an accurate mathematical model with the minimum number of degrees of freedom for describing the floating sleeper phenomenon. This was accomplished using mathematical modeling supported by extensive field measurements of the railway track. Although the observed phenomenon is very complex, the simplified single degree of freedom (SDOF) mathematical model proved accurate enough for its characterization. The progression of the deterioration of the railway track was successfully correlated to changes in the maximal dynamic factor for different types of pulse loading. The results of the presented study might enable the enhanced construction and maintenance of railroads, particularly in karst areas.

**Keywords:** floating sleepers; dynamic factor; pulse loading; field measurements; SDOF mathematical model

**MSC:** 37N15; 37N30; 74-05



**Citation:** Uranjek, M.; Imamović, D.; Peruš, I. Mathematical Modeling of the Floating Sleeper Phenomenon Supported by Field Measurements. *Mathematics* **2024**, *12*, 3142. <https://doi.org/10.3390/math12193142>

Academic Editor: Carlo Bianca

Received: 11 September 2024

Revised: 2 October 2024

Accepted: 5 October 2024

Published: 8 October 2024



**Copyright:** © 2024 by the authors. Licensee MDPI, Basel, Switzerland. This article is an open access article distributed under the terms and conditions of the Creative Commons Attribution (CC BY) license (<https://creativecommons.org/licenses/by/4.0/>).

## 1. Introduction

For a detailed analysis of the stress state in ballast railway tracks for different extreme cases such as geometrical irregularities of the rail, ballast fouling, or abrupt changes in stiffness along the railway track, realistic but also complex 2D [1] or 3D [2] numerical models are used. Simpler models, on the other hand, enable quicker characterization of the problem; however, they do not allow all factors to be considered. The simplest track model is the one introduced by Winkler in 1867, where the track was modeled as a beam on a continuous elastic foundation [3,4]. In this approach, a beam (rail) rests on a continuous elastic foundation modeled by evenly distributed linear spring stiffness. This model is suitable for assessing the static loading of a track on a soft support (i.e., wooden sleepers); however, it does not allow dynamic effects to be considered. In a more advanced approach, the track is modeled as a beam on discrete supports (e.g., Ref. [5]). Here, the rail is modeled as a Euler–Bernoulli or Rayleigh–Timoshenko beam, and rail pads by spring-damper systems. Sleepers are represented as rigid masses and ballast is modeled by spring-damper systems. To be able to consider the influence of resonance at lower frequencies, this model can be upgraded by incorporating the ballast mass [6]. The viability and applicability of this model are considered in Ref. [7] by using calibration with a 3D modeling approach. At this point, we should mention other problems that are directly related to the issues of railway infrastructure, e.g., the hunting phenomenon related to the lateral oscillation of the rail wheels [8], mathematical modeling of the deformable characteristics of railway ballast [9], and various complex mathematical analyses of the rail beam, e.g., numerical analyses of the non-uniform layered ground vibration caused by a moving railway load [10]. In the modern sustainable development of railway infrastructure, we must not forget about innovation (e.g., Cai et al. [11] identified key influencing factors in railway engineering technological innovation in complex and difficult areas) and maintenance [12–15]. Effective

planning, first, and maintenance of railway infrastructure, second, could largely prevent the phenomenon of floating sleepers discussed in this article. A step toward a better understanding of this phenomenon is, therefore, presented in this article.

The main objective of this work was to develop a simplified mathematical model with the minimum number of degrees of freedom possible, which would be accurate enough and allow simple characterization of the floating sleeper phenomenon. Such an approach would enable an easy graphical presentation of the results. Therefore, this paper could improve engineering understanding of the phenomenon and the effective development of various technical solutions to deal with the problem efficiently. Within the framework of the performed analysis, a simplified mathematical model for loading and dynamic response has been used. The results in the presented study indicate that the dynamic factor for short-term pulse loading, which corresponds to a one- or two-axle passage of train composition, has relatively low values for typical track stiffness. The factor reaches very high values with decreasing track stiffness and then decreases with a small value of track stiffness. The observed phenomenon can be described as highly non-linear.

## 2. Methods and Field Measurements

### 2.1. Basic Idea and Methods Used

Solving the problem of floating sleepers can be approached in several ways—with an experimental approach, with a theoretical approach, or with a combination of both. For example, in Ref. [16], it was established with an experimental approach that the phenomenon of floating sleepers is affected by a local change in the stiffness of the rail beam, which is generally the result of several factors. These were identified based on extensive experimental work and an analysis of the obtained results, with the help of artificial neural networks. Of the factors identified in the research, welds between two adjacent rails had by far the greatest impact (40%), while 13%, 10%, 10%, 9%, 9%, and 9% were attributed to gravel, maximum rail displacement, gauge, twist, heterogeneity, and residue, respectively. However, mathematical modeling of the phenomenon of floating sleepers according to the theoretical approach is very demanding, as is also shown by the research so far, since the existing models (e.g., Refs. [2,17]) do not yet explain the phenomenon satisfactorily. The presented research proposes a combined approach that includes the results of observations obtained through field measurements and simplified mathematical models. In this proposal, first, instead of complex discretization with MDOF models (e.g., Refs. [2,17]), which also include the half-space of the rail beam, we use simple (equivalent) SDOF models, which have all the properties and loadings of the considered rail beam structure. In this way, the individual influences and states of the considered system can be identified more easily. Furthermore, the obtained results of SDOF models in the form of simpler mathematical expressions can be more effectively interpreted and understood in engineering terms. Based on the obtained results measured in the field, such a model can be calibrated relatively easily. In this way, SDOF models will not accurately summarize all the characteristics of the phenomenon, but they will enable simpler calculations and help in understanding and solving the problems of floating sleepers.

Figure 1 shows the progression of the floating sleeper phenomenon on a short stretch of track. An indicator of the beginning of the phenomenon is a slight local dusting in the vicinity of the affected sleeper (Figure 1, left). As the phenomenon progresses, dusting intensifies and can also spread to adjacent sleepers (Figure 1, top right). The final stage of the phenomenon, when the sleepers lose contact with the ground and individual sleepers practically hang from the rails, is shown in Figure 1, bottom right.

Ballast fouling reveals a change in some of the material characteristics of the track, e.g., the reduction in stiffness over time within the observed period, which, in principle, signifies the non-linear behavior of the observed phenomenon.

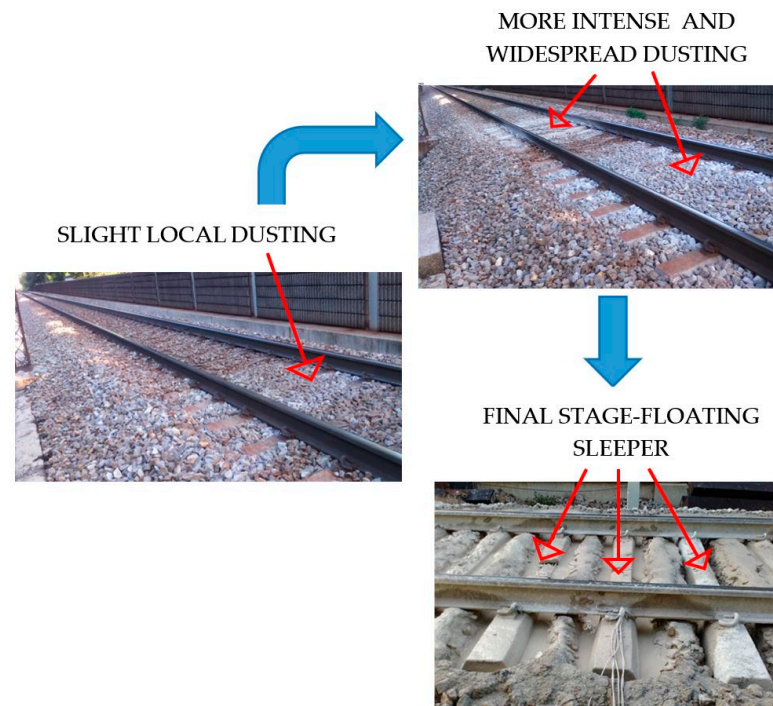


**Figure 1.** Progression of the floating sleeper phenomenon in various states on a short stretch of track.

## 2.2. Assumptions, Equations, and Simplified SDOF Dynamic Model

### 2.2.1. Basic Assumptions

Using the simplified SDOF mathematical model, in comparison with more accurate MDOF models (e.g., Ref. [17]), we considered the following assumptions, considering the facts found in the field:

- The passage of the axle of the train composition over the observed location in the idealized simplified mathematical model represents a special case of short-term pulse loading.
- In the model, a single spring is considered between the axle of the train composition, which causes the load, and the track, which carries this load.
- In the case of short-term pulse loadings, due to their relatively short-term action, the damping in the basic equation of motion can be neglected, because it has little effect on the response. Such an approach at the same time greatly simplifies the solution of the problem.
- Since we are interested in the change of influence and the effects at the location of short-term pulse loading, we neglect the influence of adjacent structural elements in the SDOF model. In this way, the absolute values of the response are somewhat imprecisely determined. However, the qualitatively calculated response still realistically describes the actual situation, especially in the case when the stiffness characteristics of the SDOF model are calibrated with actual measurements and findings from the literature.
- Since observations in the field (Figures 1 and 2) unequivocally show that the floating sleeper is a non-linear phenomenon, it should also be modeled mathematically. This would not be a problem to analyze on a simple SDOF system; a bigger problem is to predict in advance the material characteristics of the track at the considered location. For the sake of simplification and easier physical interpretation of the results, the various most probable loadings for the entire range of real values of the oscillation times of the considered structure and duration of pulse loadings were analyzed.
- The observed phenomenon is non-linear; regardless, it was treated as a linear system in discrete time windows with known (i.e., assumed) values of stiffness and mass. In most cases, stiffness and mass values change between individual discrete time points.

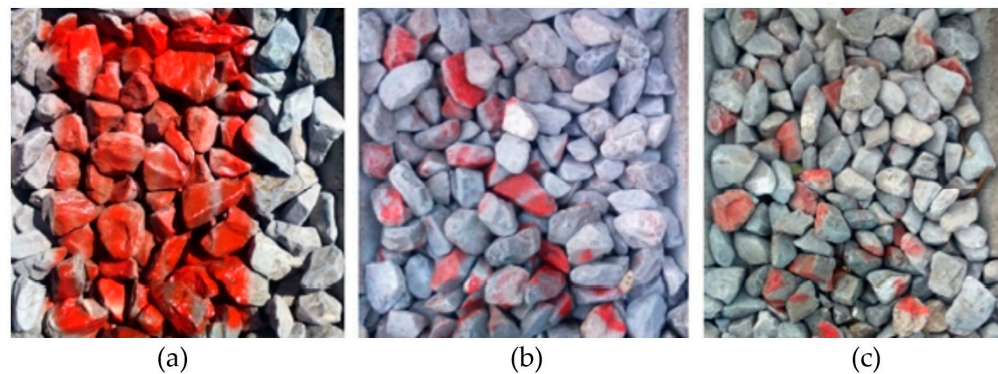


**Figure 2.** Damage of ballast in a location prone to the phenomenon of floating sleepers: (a) initial state after identification, (b) damaged state after 21 days, and (c) damaged state after an additional 21 days.

Figure 2 shows the different states of ballast at the location of the floating sleeper over time and the high cycle “fatigue” of the ballast track material. There is a flow of material (i.e., ballast) whereby the individual stones of the ballast behave similarly to molecules in a liquid, except that, here, the stones are of very different shapes and dimensions; unlike a normal liquid, individual stones also wear out during translational and rotational movement. This wearing down of the ballast changes its contribution to the stiffness of the system under consideration; in this specific case, the stiffness of the track decreases—the greater the wear, the lower the stiffness of the track. The last finding confirms again that the observed phenomenon is (highly) non-linear. For the needs of our simplified SDOF mathematical model, it is crucial that the considered phenomenon can be described in various short time windows with the corresponding values of the (constant) terms of the differential equation (e.g., Ref. [18]), as will be described below.

### 2.2.2. Equations of Motion

The behavior of the observed structure under the action of an external time-varying loading can be described by the equation of motion for discrete models with multiple degrees of freedom (MDOF) (e.g., Refs. [17,18]):

$$[M]\{\ddot{U}\} + [C]\{\dot{U}\} + [K]\{U\} = \{f(t)\}, \quad (1)$$

where  $[M]$ ,  $[C]$ , and  $[K]$  represent mass, damping, and the stiffness matrix, respectively;  $\{\ddot{U}\}$ ,  $\{\dot{U}\}$  and  $\{U\}$  represent acceleration, velocity, and displacement vectors, respectively, and  $\{f(t)\}$  represents the loading vector.

For simple systems, i.e., single degree of freedom (SDOF) models, an algebraic form of Equation (1) can be written as:

$$m \ddot{u} + c \dot{u} + k u = f(t), \quad (2)$$

where  $m$ ,  $c$ , and  $k$  represent mass, damping, and stiffness, respectively;  $\ddot{u}$ ,  $\dot{u}$  and  $u$  represent acceleration, velocity, and displacement, respectively, and  $f(t)$  represents dynamic loading.

Solving the homogeneous part of the differential Equation (2) defines the basic dynamic parameter of the structure under consideration, which is called the period of the structure and can be expressed as:

$$T = 2\pi \sqrt{\frac{m}{k}}. \quad (3)$$

### 2.2.3. Dynamic Factor of the SDOF System

Generally, we are interested in the maximum values of individual observed quantities. Since the displacements of the structure are directly proportional to the forces of the structure, we usually define the maximal dynamic factor,  $D_{f,max}$  (known also as the maximal deformation response factor, i.e., Ref. [18]), with the equation:

$$D_{f,max} = \frac{u_{max}}{u_0}, \tag{4}$$

where  $D_{f,max}$  represents the ratio between the maximum absolute value of the displacements ( $u_{max}$ ) during the time-history response, described by Equation (2), and the absolute value of the displacement at static loading ( $u_0$ ), which is usually determined as the amplitude of the dynamic loading. With the known value of  $D_{f,max}$ , the maximum dynamic influences on the structure can be treated as static, which significantly simplifies solving and understanding the problem.

### 2.2.4. Different Pulse Loadings of the SDOF System

Short-duration pulse loadings are generally described by various functions, with the key characteristic of such a loading being that its relative duration is short. Here, the parameter  $\lambda = \bar{t}/T$  refers to the ratio between the duration of the short-term pulse loading ( $\bar{t}$ ) and the period of the structure ( $T$ ). Equation (2) is simplified in this case—since the influence of damping is negligible for pulse loading, the term  $c\dot{u}$  can be neglected. Moreover, since the influence of damping is neglected, the transmissibility (which represents the factor that tells how much loading is transmitted to the ballast; see, e.g., Ref. [10]) can be described by the dynamic factor (Equation (4)).

Completed solutions for  $D_{f,max}$  in the case of rectangular pulse loading (Figure 3a) are given in Ref. [18]. The solution is relatively simple and can be written in its closed form as:

$$D_{f,max} = \frac{u_{max}}{u_0} = \begin{cases} 1 - \cos(2\pi \lambda) & \lambda \leq \frac{1}{2} \\ 2 & \lambda \geq \frac{1}{2} \end{cases}. \tag{5}$$

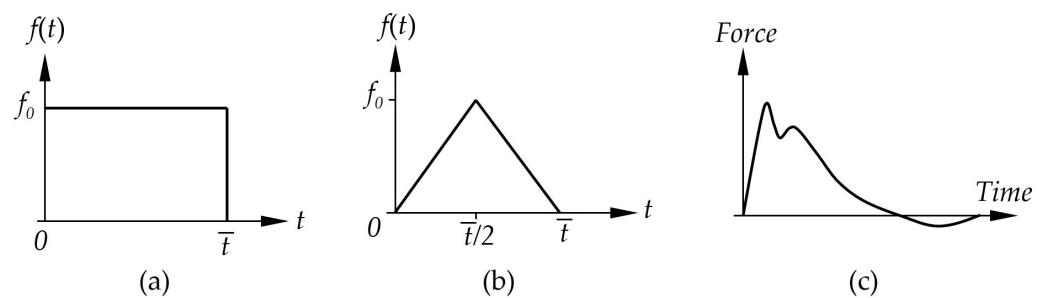


Figure 3. Different pulse loadings: (a) rectangular, (b) symmetric triangular, and (c) general loading.

Symmetric triangular pulse loading (Figure 3b) is more complicated as it includes the calculation of the response in three areas (the rising part of the pulse on the left, the falling part of the pulse on the right, and no pulse on the right). To make it easier to understand the results of later derivations which type of pulse loading is more suitable for the simulation of the actual load when the axle of the train composition passes over the observed track, a full derivation is given here. In the derivation, we proceed from Equation (2), noting that the displacement  $u(t) = u_0 \cdot D_f(t)$  is the product of static displacement and the dynamic factor, and the loading function  $f(t) = f_0 \cdot D_L(t)$  is the product of static loading and the dynamic loading factor of the symmetric triangular pulse loading. Equation (2) is further written as:

$$m \cdot u_0 \cdot \ddot{D}_f(t) + k \cdot u_0 \cdot D_f(t) = f_0 \cdot D_L(t). \tag{6}$$

Dividing Equation (6) by  $m \cdot u_0$  and considering  $\frac{f_0}{u_0} = k$  and  $\frac{k}{m} = \omega^2$ , the following is obtained:

$$\ddot{D}_f(t) + \omega^2 \cdot D_f(t) = \omega^2 \cdot D_L(t), \tag{7}$$

where the dynamic factor of the symmetric triangular load  $D_L(t)$  is defined as:

$$D_L(t) = \begin{cases} \frac{2 \cdot t}{\bar{t}} & \text{for } 0 \leq t \leq \frac{\bar{t}}{2} \\ 2 - \frac{2 \cdot t}{\bar{t}} & \text{for } \frac{\bar{t}}{2} \leq t \leq \bar{t} \\ 0 & \text{for } t > \bar{t} \end{cases} \tag{8}$$

Next, the time-history response of the dynamic factor in three phases is determined. The dynamic factor for the first phase (I), considering the initial conditions  $D_f^I(t = 0) = 0$  and  $\dot{D}_f^I(t = 0) = 0$ , is given by:

$$D_f^I(t) = \frac{2 \cdot (t \cdot \omega - \sin(t \cdot \omega))}{\bar{t} \cdot \omega} \quad 0 \leq t \leq \frac{\bar{t}}{2}, \tag{9}$$

and

$$\dot{D}_f^I(t) = \frac{2 - 2 \cdot \cos(t \cdot \omega)}{\bar{t}} \quad 0 \leq t \leq \frac{\bar{t}}{2}. \tag{10}$$

The solution for the dynamic factor in the second phase (II), considering the initial conditions  $D_f^{II}(t = \frac{\bar{t}}{2}) = D_f^I(t = \frac{\bar{t}}{2})$  and  $\dot{D}_f^{II}(t = \frac{\bar{t}}{2}) = \dot{D}_f^I(t = \frac{\bar{t}}{2})$ , is:

$$D_f^{II}(t) = \frac{2 \cdot \left( 2 \cdot \sin\left(t \cdot \omega - \frac{\bar{t} \cdot \omega}{2}\right) - \omega \cdot (t - \bar{t}) - \sin(t \cdot \omega) \right)}{\bar{t} \cdot \omega} \quad \frac{\bar{t}}{2} \leq t \leq \bar{t}, \tag{11}$$

and

$$\dot{D}_f^{II}(t) = \frac{2 \cdot \left( 2 \cdot \cos\left(t \cdot \omega - \frac{\bar{t} \cdot \omega}{2}\right) - \cos(t \cdot \omega) - 1 \right)}{\bar{t}} \quad \frac{\bar{t}}{2} \leq t \leq \bar{t}. \tag{12}$$

The solution for the dynamic factor in the third phase (III), considering the initial conditions  $D_f^{III}(t = \bar{t}) = D_f^{II}(t = \bar{t})$  and  $\dot{D}_f^{III}(t = \bar{t}) = \dot{D}_f^{II}(t = \bar{t})$ , is:

$$D_f^{III}(t) = \frac{8 \cdot \sin^2\left(\frac{\bar{t} \cdot \omega}{4}\right) \sin\left(t \cdot \omega - \frac{\bar{t} \cdot \omega}{2}\right)}{\bar{t} \cdot \omega} \quad t > \bar{t}, \tag{13}$$

and

$$\dot{D}_f^{III}(t) = \frac{\cos\left(t \cdot \omega - \frac{\bar{t} \cdot \omega}{2}\right) \cdot 8 \sin^2\left(\frac{\bar{t} \cdot \omega}{4}\right)}{\bar{t}} \quad t > \bar{t}. \tag{14}$$

The time at which the maximal dynamic factor occurred for the first phase is then determined. From Equation (6), it follows:

$$\dot{D}_f^I(t) = \frac{2 - 2 \cdot \cos(\omega \cdot t)}{\bar{t}} = 0 \rightarrow \cos(\omega \cdot t) = 1 \rightarrow \omega \cdot t = 2 \cdot \pi \cdot n. \tag{15}$$

Considering  $T = \frac{2 \cdot \pi}{\omega}$ , the time is thus:

$$t_n^I = T \cdot n; \quad n = 1, 2, 3 \dots \tag{16}$$

Only solutions within the interval  $0 \leq t \leq \frac{\bar{t}}{2}$  are considered; given that  $\bar{t} = \lambda \cdot T$ , the condition is:

$$\lambda \geq 2 \cdot n. \tag{17}$$

Substituting Equation (16) into Equation (9), the extreme value of the dynamic factor is obtained:

$$D_{f,\max}^I = D_f^I(t_n^I = T) = \frac{2 \cdot n}{\lambda} \quad \lambda \geq 2 \cdot n; \quad n = 1, 2, 3 \dots \quad (18)$$

Next, the time at which the maximal dynamic factor occurred for the second phase is determined, derived from Equation (12) under the condition  $\dot{D}_f^{II}(t) = 0$ . The expression follows:

$$2 \cdot \cos\left(t \cdot \omega - \frac{\bar{t} \cdot \omega}{2}\right) - \cos(t \cdot \omega) - 1 = 0. \quad (19)$$

Considering  $T = \frac{2 \cdot \pi}{\omega}$ , the general four solutions of time obtained from Equation (19) are:

$$\begin{aligned} t_{1,n}^{II} &= T \cdot (n - \alpha_1) \\ t_{2,n}^{II} &= T \cdot (n + \alpha_2) \\ t_{3,n}^{II} &= T \cdot (n - \alpha_2) \\ t_{4,n}^{II} &= T \cdot (n + \alpha_1) \end{aligned} \quad n = 1, 2, 3 \dots, \quad (20)$$

where  $\alpha_i$  ( $i = 1, 2$ ), in Equation (20), is defined as:

$$\alpha_i = \frac{1}{2\pi} \cdot \cos^{-1} \left( \frac{1}{2} \cdot \left( \frac{3 + (-1)^i \left( 4\sqrt{2} \cos\left(\frac{\pi \cdot \bar{t}}{2T}\right) - 4\sqrt{2} \cos\left(\frac{3\pi \cdot \bar{t}}{2T}\right) \right)}{5 - 4 \cos\left(\frac{\pi \cdot \bar{t}}{T}\right)} - 1 \right) \right). \quad (21)$$

Only solutions within the interval  $\frac{\bar{t}}{2} \leq t = t_{i,n}^{II} \leq \bar{t}$  are considered; given that  $\bar{t} = \lambda \cdot T$ , the condition is:

$$\frac{\lambda}{2} \leq \frac{t_{i,n}^{II}}{T} \leq \lambda. \quad (22)$$

From Equation (22), the lower and upper bounds of parameter  $\lambda$  for time  $t_{i,n}^{II}$  are determined. Substituting time  $t_{i,n}^{II}$  from Equation (20) into Equation (11),  $D_{f,\max}^{II} = D_f^{II}(t = t_{i,n}^{II})$  is obtained. Among all possible solutions, only the envelope of maximal dynamic factor values up to a parameter of  $\lambda = 10$  is listed here.

$$D_{f,\max}^{II} = \begin{cases} D_f^{II}(t = t_{4,0}^{II}) & 0.0 \leq \lambda \leq 0.5 \\ D_f^{II}(t = t_{1,1}^{II}) & 0.5 \leq \lambda \leq 2.0 \\ D_f^{II}(t = t_{2,1}^{II}) & 2.0 \leq \lambda \leq 2.5 \\ D_f^{II}(t = t_{3,2}^{II}) & 2.5 \leq \lambda \leq 4.0 \\ D_f^{II}(t = t_{4,2}^{II}) & 4.0 \leq \lambda \leq 4.5 \\ D_f^{II}(t = t_{1,3}^{II}) & 4.5 \leq \lambda \leq 6.0 \\ D_f^{II}(t = t_{2,3}^{II}) & 6.0 \leq \lambda \leq 6.5 \\ D_f^{II}(t = t_{3,4}^{II}) & 6.5 \leq \lambda \leq 8.0 \\ D_f^{II}(t = t_{4,4}^{II}) & 8.0 \leq \lambda \leq 8.5 \\ D_f^{II}(t = t_{1,5}^{II}) & 8.5 \leq \lambda \leq 10. \end{cases} \quad (23)$$

Next, the time at which the maximal dynamic factor occurs for the third phase is determined, derived from Equation (14) under the condition  $\dot{D}_f^{III}(t) = 0$ . The expression follows:

$$\cos\left(t \cdot \omega - \frac{\bar{t} \cdot \omega}{2}\right) \cdot \sin^2\left(\frac{\bar{t} \cdot \omega}{4}\right) = 0. \quad (24)$$

Considering  $T = \frac{2 \cdot \pi}{\omega}$ , the general time solution  $t_{i,n}^{III}$  is:

$$t_{i,n}^{III} = \frac{t_1}{2} + T \cdot \left( n - \frac{(-1)^i}{4} \right) \quad i = 1, 2 \text{ and } n = 1, 2, 3 \dots \quad (25)$$

Furthermore, only solutions within the interval  $t = t_{i,n}^{III} > \bar{t}$  are considered; given that  $\bar{t} = \lambda \cdot T$ , the condition is:

$$0 \leq \lambda < 2n - \frac{(-1)^i}{2} \quad i = 1, 2 \text{ and } n = 1, 2, 3 \dots \tag{26}$$

Considering time  $t_{i,n}^{III}$  from Equation (25) in Equation (13), it follows:

$$D_{f,\max}^{III} = D_f^{III}(t = t_{i,n}^{III}) = \frac{2 \cdot \cos(\pi \cdot \lambda) - 2}{(-1)^i \cdot \pi \cdot \lambda} \tag{27}$$

From Equation (27), it can be observed that the magnitude of the dynamic factor  $D_{f,\max}^{III}$  is independent of  $n$ . Additionally, it is evident that the dynamic factor for  $i = 2$  is negative; thus, only the dynamic factor values for  $i = 1$  are of interest. The dynamic factor for phase (III) is, therefore:

$$D_{f,\max}^{III} = D_f^{III}(t = t_{1,n}^{III} = t_1^{III}) = \frac{2 - 2 \cdot \cos(\pi \cdot \lambda)}{\pi \cdot \lambda} \text{ for } \lambda \geq 0. \tag{28}$$

It can be observed from Figure 4 that for phase III of the load application, the maximal dynamic factor occurs only within the interval  $0 \leq \lambda \leq 0.5$ . For the remaining interval  $0.5 \leq \lambda \leq 10$ , the maximal dynamic factor occurs during phase II of the load application.

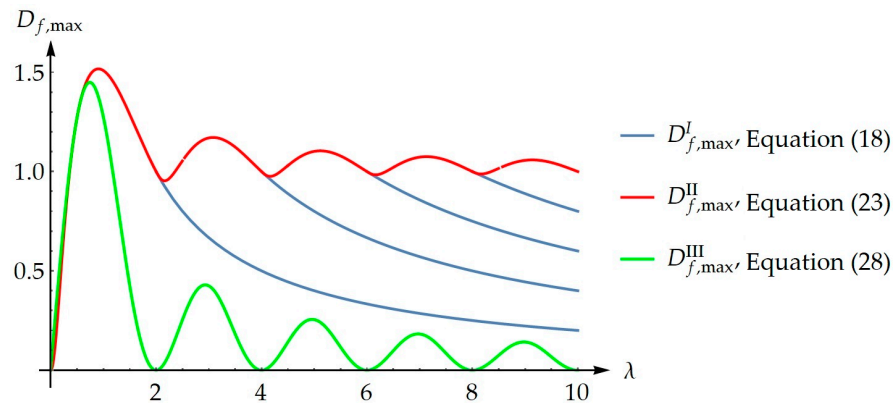
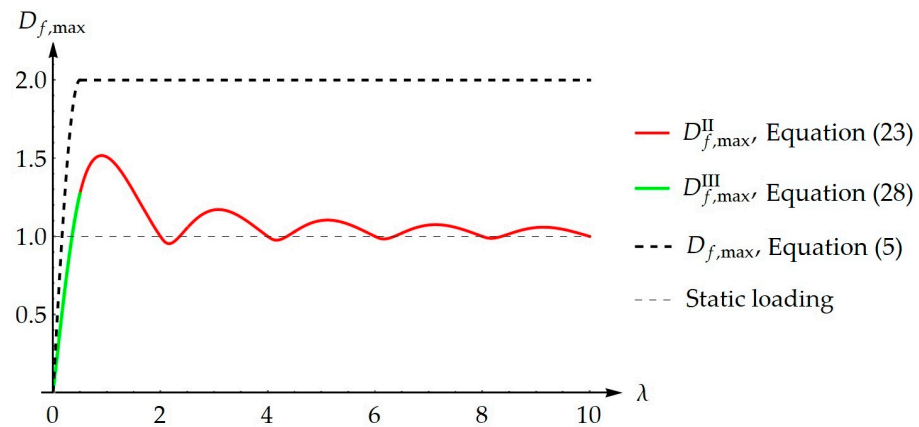


Figure 4. Maximal dynamic factor for all three phases of symmetric triangular pulse loading.

Thus, based on the dynamic factors for all three phases of load application, the final envelope  $D_{f,\max}$  for the interval  $0 \leq \lambda \leq 10$  is constructed in Equation (29), which is also graphically shown in Figure 5.

$$D_{f,\max} = \begin{cases} D_f^{III}(t = t_1^{III}) & 0.0 \leq \lambda \leq 0.5 \\ D_f^I(t = t_{1,1}^I) & 0.5 \leq \lambda \leq 2.0 \\ D_f^I(t = t_{2,1}^I) & 2.0 \leq \lambda \leq 2.5 \\ D_f^I(t = t_{3,2}^I) & 2.5 \leq \lambda \leq 4.0 \\ D_f^I(t = t_{4,2}^I) & 4.0 \leq \lambda \leq 4.5 \\ D_f^I(t = t_{1,3}^I) & 4.5 \leq \lambda \leq 6.0 \\ D_f^I(t = t_{2,3}^I) & 6.0 \leq \lambda \leq 6.5 \\ D_f^I(t = t_{3,4}^I) & 6.5 \leq \lambda \leq 8.0 \\ D_f^I(t = t_{4,4}^I) & 8.0 \leq \lambda \leq 8.5 \\ D_f^I(t = t_{1,5}^I) & 8.5 \leq \lambda \leq 10. \end{cases} \tag{29}$$





**Figure 5.** Envelope of the maximal dynamic factor of all three phases of symmetric triangular and rectangular pulse loading, respectively.

### 2.3. Performed Measurements

#### 2.3.1. Measurement of Vertical Loads by Train Crossings

The vertical load transmitted by every single axle of the train in transit over the track was measured by the Marini SMCV measurement system. The layout of the Marini measuring system is shown in Figure 6. The system enables the measurement of:

- Dynamic or quasi-static vertical loads transmitted by each wheel/axle of the train.
- Each axle speed of the train in transit.
- The distance between two consecutive axles of the train in transit.
- Evaluation of an eventual excessive load on an axle compared to a set threshold value.
- Evaluation of an unbalanced load between the two wheels of the same axle, relative to a set threshold.



**Figure 6.** Layout of the Marini SMCV measuring system on the railway track.

#### 2.3.2. Measurements of the Displacement of Sleepers

For displacement measurements (Figure 7), inductive displacement sensors were used, which made it necessary to provide a stationary reference structure. Because of this, a cantilevered scaffolding was made at each measuring point, placed about 3 m from the tracks in an area where the ground vibration amplitude due to the passing of trains was negligible in comparison to the vertical displacement amplitudes of the observed railway sleepers.



**Figure 7.** Measurements of the displacement of sleepers using inductive displacement sensors.

### 2.3.3. Measurements of Strain in the Rails

For measurements of strain on the rail (Figure 8), strain gauges were used. Before applying strain gauges to the rail surface using a special glue, the surface was smoothed and deoiled. When the surface of the structure that is the subject of measurements is deformed, the foil is also deformed, causing its electrical resistance related to strain by gauge factor to change. Consequently, strains and stresses can be calculated from the measured electrical resistance.

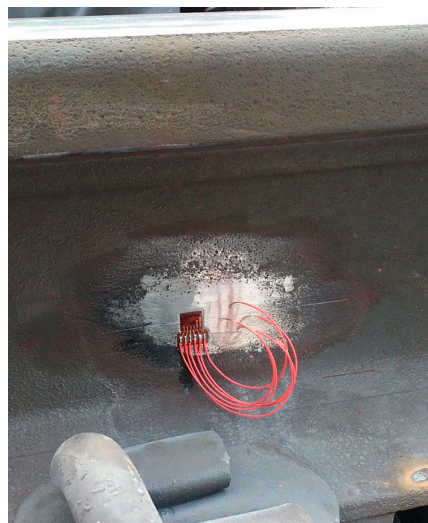


**Figure 8.** Strain gauge applied to the rail surface.

## 3. Results

### 3.1. Measured Loadings—Results of Load Analysis and Responses of the Rail Track

As part of the field measurements, stresses in the middle of the rail above the considered sleeper were evaluated. Based on the measured vertical normal stresses, a relatively accurate form of loading acting on the sleeper has been obtained, especially compared to previous authors who determined the final shape and length of the loading using a genetic algorithm [18].

#### 3.1.1. Stresses in the Rail Due to the Passage of Locomotives

As the locomotive passed the measurement location, measurements were taken for all four axles. Figure 9 shows stresses  $\sigma_x$ ,  $\sigma_y$ , and  $\tau_{xy}$  during the locomotive's first and fourth axles passing over the measuring point. In both measurements, a time interval of 0.25 s

is considered, from 16.15 to 16.40 s for axle 1 transition measurements, and from 16.86 to 17.11 s for axle 4 transition measurements. As expected, stresses are at their maximum when the locomotive axle is above the measurement point. At the passage of axle 1, i.e., at 16.30 s, stresses  $\sigma_x$  amount to 8.516 N/mm<sup>2</sup>, while at the transition of axle 4 (at 17.00 s), they reach a value of 14.82 N/mm<sup>2</sup>. In the case of vertical normal stresses  $\sigma_y$ , the highest value of 34.64 N/mm<sup>2</sup> was measured directly after the transition of axle 1 at a time of 16.3033 s. At the transition of axle 4 at a time of 17.00 s, a smaller value of 18.25 N/mm<sup>2</sup> was measured. In Figure 9, shear stresses  $\tau_{xy}$  are equal to zero during the passage of axle 1 at the time of 16.30 s, when the axle is exactly above the measuring point, and reach their extremes immediately before and right after axle 1 passes over the measuring point; at 16.295 s, the measured value is 20.18 N/mm<sup>2</sup> and, in 16.3067 s, the value of  $-23.77$  N/mm<sup>2</sup> is reached. Also, in the transition of axle 4, the sign of the shear stresses immediately before and after the transition is inverted, and the shear stress order of magnitude approximately coincides with the values measured in the transition of axle 1.

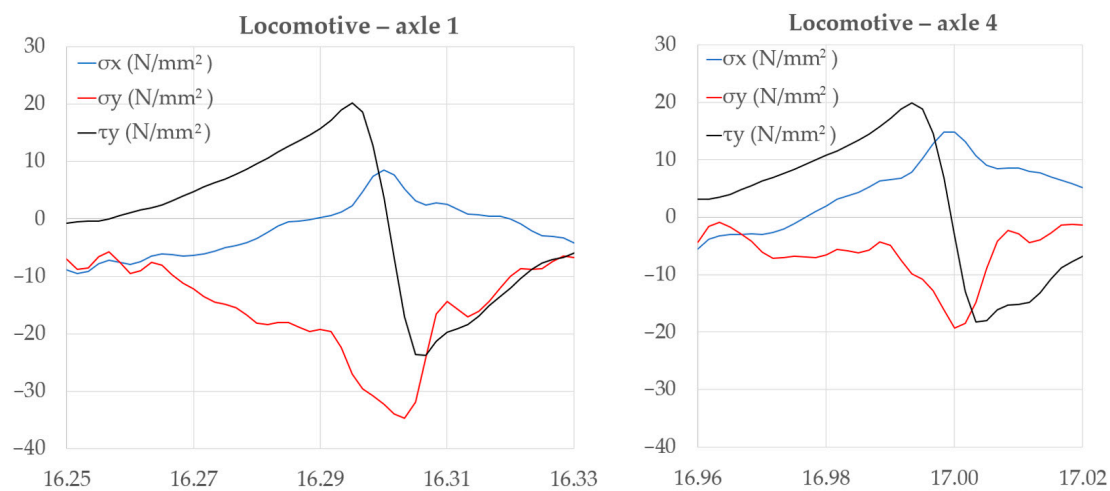


**Figure 9.** Stresses measured in the rail surface when axle 1 of the locomotive (left) and axle 4 of the locomotive (right) passed over the measuring point.

As can be seen, the shape of measured vertical stress  $\sigma_y$  coincides well with the triangular pulse loading considered in the numerical models used by other researchers. If the values measured in the passing of axle 1 and axle 4 are compared, one can acknowledge the effect of the first axle in the pair influencing the results of a neighboring axle passing through the measuring point. Vertical force at the rail–wheel contact point tends to lift the rail and sleeper at some distance from the contact point. Consequently, the passage of axle 3 influences the reduction in stresses measured by the passage of axle 4.

### 3.1.2. Stresses in the Rail Due to Passage of Carriages

Stresses in the rail were also measured and analyzed during the passage of train carriages. Figure 10 shows the stress curves  $\sigma_x$ ,  $\sigma_y$ , and  $\tau_{xy}$  during the passage of the first axle of the first carriage and the rear (140th) axle of the last carriage in the train composition over the measuring point. Like the measurements at the passage of the first axle of the locomotive, here, also, the normal stresses  $\sigma_x$  and  $\sigma_y$  and the shear stress  $\tau_{xy}$  coincide well. The change in shear stresses  $\tau_{xy}$  can serve as an indicator of the passage of the axle over the measuring point. During the passage of axle 1 of the first carriage in the train composition (Figure 10, left), the maximum value of the measured vertical displacement occurs slightly before (at approximately 0.03 s) the onset of extreme stress. This can be attributed to the influence of the displacements of those sleepers adjacent to the sleepers directly at the measuring point or to the time-dependent relaxation of the elements and materials of the rail track. As expected, the measured values are smaller compared to the passage of the

locomotive. Horizontal stresses reach an extreme at the time of 17.257 s, i.e., 3.445 N/mm<sup>2</sup>, and the vertical normal stresses  $\sigma_y$  reach an extreme at the time of 17.287 s at a value of 16.673 N/mm<sup>2</sup>, which is approximately half the value measured during the passage of the first axle of the locomotive.

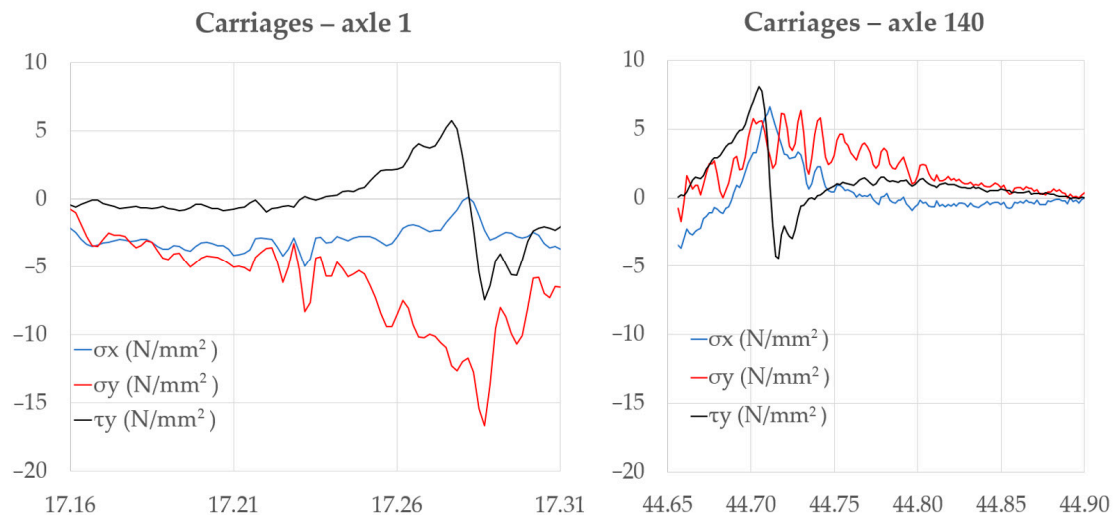


**Figure 10.** Stresses measured in rail surface during the passage of axis 1 of the first carriage in the train composition (**left**) and the last—140th—axle of the last wagon (**right**) over the measuring point.

### 3.2. Simulated Loadings and Corresponding Deformation Response Factors

The experimental measurements from Section 3.1 confirmed the theories other researchers have already considered (i.e., Ref. [19]). Namely, the actual load caused by the individual axle of the train composition when passing the observed place has an approximately symmetrical shape, which, in the first rough approximation, resembles a symmetrical, triangular shape (Figure 3b). Most of the actual loading, however, corresponds to the double triangular form, as freight wagons generally have two axles at the beginning and end of each wagon. Generally, the shape of the pulse loading must be described with a more complex function than a linear one.

Based on the displayed results of the field measurements and axle loading proposed in Ref. [19], the values of the maximal dynamic factors for different pulse loading following the procedure in Section 2.2 were calculated. Thus, all the applied loads are symmetric pulse loadings. They differ in whether it is a single or double pulse and in the shape of the function that describes the rising and falling part. Definitions and designations of pulse loadings were summarized and expanded according to Ref. [19]. Thus, all four pulse loadings can be defined and denoted as:

- **SPL-L:** single-pulse loading of linearly distributed load that decreases symmetrically concerning the geometric center of the wheel.
- **DPL-L:** double-pulse loading of linearly distributed load that decreases symmetrically for the geometric center of the wheel.
- **SPL-Q:** single-pulse loading of quadratically distributed load that decreases symmetrically concerning the geometric center of the wheel.
- **DPL-Q:** double-pulse loading of quadratically distributed load that decreases symmetrically to the geometric center of the wheel.

It should be noted that the proposed shape of pulse loading in Ref. [19] was inspired by the single wheel-induced displacement field. In Figure 11, the distribution of vertical normal stresses is shown and compared to the proposed simulated pulse loadings in this paper. Observed differences can be attributed to the influence of the multiple axle passages of a train composition. The basic data for the three supplementary impulse loads (SPL-Q, DPL-L, and SPL-Q) and the corresponding dynamic factors ( $D_{f,max}$ ) were obtained using

the same methodology as that employed for the SPL-L case in Section 2.2. The results for the dynamic factors in all four cases are shown in Figure 12.

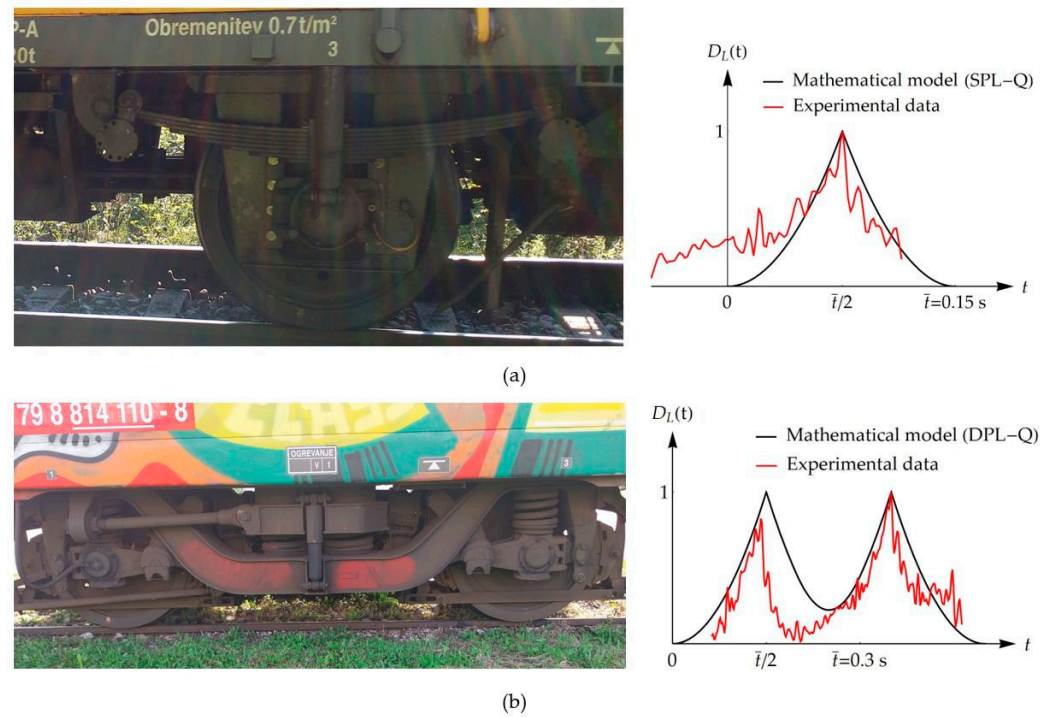


**Figure 11.** Normalized measured vertical normal stresses in the rail for the (a) one-axle and (b) two-axle passage of the train composition and their approximations for pulse loadings in the SDOF mathematical model.

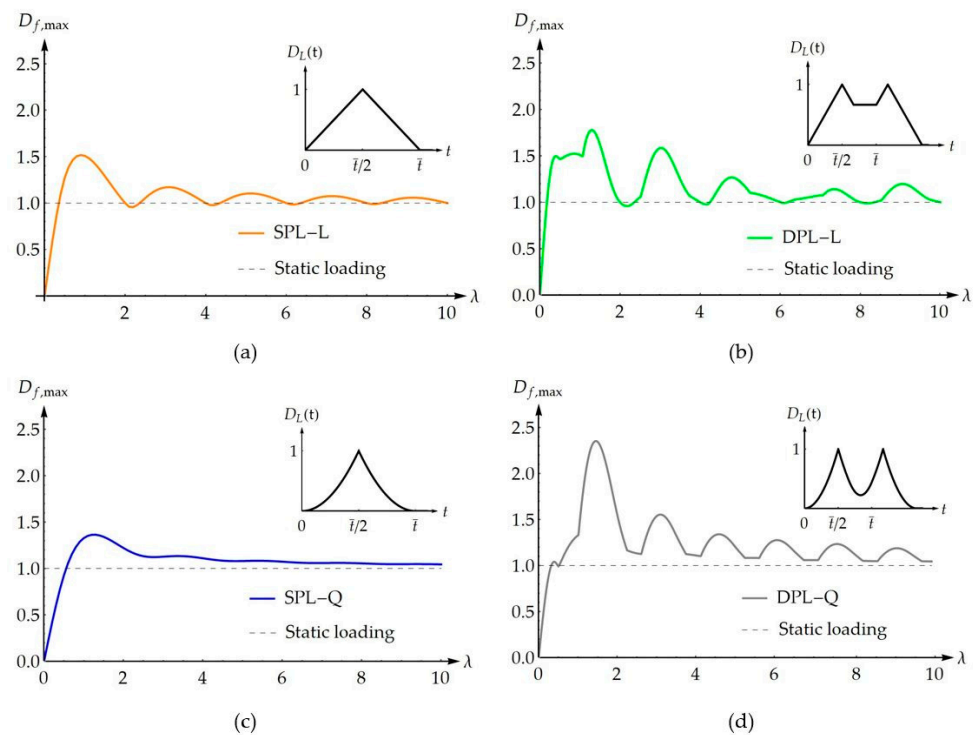


**Figure 12.** Different pulse loadings and the corresponding envelopes of the maximal dynamic factor of (a) SPL-L pulse loading, (b) DPL-L pulse loading, (c) SPL-Q pulse loading, and (d) DPL-Q pulse loading.

### 3.3. Results for the Maximal Dynamic Factor ( $D_{f,max}$ ) Obtained by a Simplified SDOF System

The results for the dynamic factor and Figure 13 show that the maximum value (peak) of the maximum dynamic factor increases significantly with double-pulse loading. Even on average, double-pulse loadings give higher values than single ones. One of the key results of the analysis is the identification of the highest peak in the initial part of the graph, where the position of the peak is highly dependent on the type of pulse loading. We can conclude that in the initial (ideal) state, the construction of the track is relatively rigid, as is determined (and required) by the existing regulations.

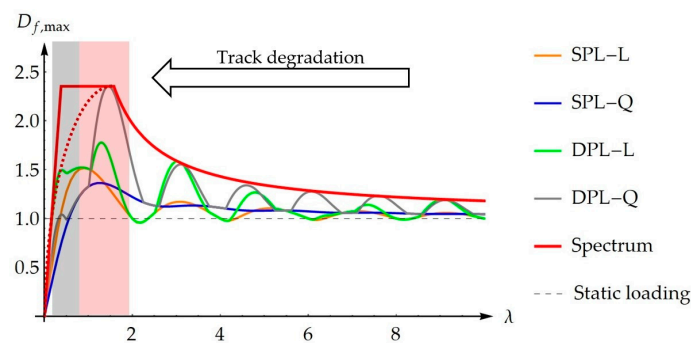


Figure 13. Comparison of the different envelopes of maximal dynamic and smoothed spectrum.

A relatively small change (reduction) in stiffness can result in a higher dynamic factor due to various influences (which have been described in the Introduction, e.g., Ref. [16]). These increase markedly with a greater reduction (large gradients of the envelope of the maximum dynamic factor) and can reach values of up to 2.5 for various pulse loadings. Such high dynamic factors in high-cycle fatigue mean high loads on the track, especially on the sleepers. The first indicator of this influence (with an increase in the dynamic factor) is mild dusting in the vicinity of the sleeper, then the dusting locally intensifies and (may) also spread to the neighboring sleepers, until the sleepers lose contact with the base and the individual sleepers practically hang from the rails (see Figure 1). With ballast fouling and the occurrence of the floating sleeper phenomenon, the stiffness is reduced significantly, which increases parameter  $\lambda$ . Consequently, the dynamic factor reduces to the values that are closest to the static case. Deterioration, which is a consequence of dynamic behavior, practically stops. However, the railway track is significantly damaged, due to the ballast fouling and the induced large displacements, and it urgently needs reconstruction.

The gray area indicates the  $\lambda$  range for the final state of the floating sleeper phenomenon, while the red area indicates the  $\lambda$  range of  $D_{f,max}$  peaks for all four pulse loadings. It is evident that the phenomenon is highly non-linear and, as such, is hard to understand in classical engineering terms, which are related to the track’s elastic characteristics. The smoothed spectrum  $S(\lambda)$  is also proposed for the maximal dynamic factor of pulse loadings, which were considered in the presented study. For small  $\lambda$  values, the smoothed spectrum is bounded by  $D_{f,max}$ , calculated for DPL-Q pulse loading. It can also be observed that the proposed smoothed spectrum, which is defined by Equation (30), will, in most instances, bound the  $D_{f,max}$  of DPL-Q pulse loading. Note that the dashed curve represents an alternative for a smoothed spectrum for  $\lambda$  values smaller than 1.58.

$$S(\lambda) = \begin{cases} 6.187 \cdot \lambda & \text{for } 0 \leq \lambda \leq 0.38 \\ 2.352 & \text{for } 0.38 \leq \lambda \leq 1.58 \\ 1.037 + \frac{1.356}{\lambda^{-0.549}} & \text{for } 1.58 \leq \lambda \leq 10 \end{cases} \quad (30)$$

## 4. Discussion

### 4.1. Discussion of the Results Obtained by Field Measurement

In the case of the generally “clean” passage of a single axle of the train composition across the measurement site, a direct correlation between the maximum loading transmitted

to the rail and the stresses (and displacements) may be seen. Such is, for example, the situation in the transition of the first axle of the locomotive and the axles of heavier wagons following lighter carriages. In the case of other axles, the influence of the load transfer via the adjacent sleepers becomes more important, and the correlation between maximum loading and stress flow is less obvious. This corresponds to the general laws of structural dynamics in discrete systems with several degrees of freedom, where the extremes of individual quantities do not occur at the same time.

#### 4.2. Discussion of the Results Obtained with the Simplified SDOF Model

The proposed simplified SDOF mathematical model includes some assumptions and observations from field measurements, which allowed relatively simple modeling of the otherwise extremely complex phenomenon of floating sleepers. The results for the maximal dynamic factor show that the maximum values are possible with double loading, regardless of its shape or type. Non-linear forms of pulse loading generally result in higher values of the maximal dynamic factor. In the initial state, which corresponds to the ideal state of a newly built track (or the existing state, which is determined by modern regulations), the stiffness of the track is relatively high. The corresponding parameter  $\lambda$  is relatively high (the right-hand side of the graph in Figure 13) and the related maximal dynamic factor is small. Any change in the properties of the track that causes a decrease in its stiffness generally increases the value of the maximal dynamic factor. An increased maximal dynamic factor causes adverse effects on the track, manifesting themselves first as local dusting (which additionally reduces stiffness). Local dusting extends to the area of a larger number of sleepers, further reducing stiffness and increasing the value of the maximal dynamic factor. Due to the high values of the dynamic factor, the effects on the railway track are increasingly pronounced (red area in Figure 13), which finally manifests itself in the fouling of the ballast, which is the last stage of the floating sleeper phenomenon. In the last stage, the stiffness of the track continues to decrease, which results in a decrease in the value of the maximal dynamic factor (gray area in Figure 13). The phenomenon that now occurs in the equilibrium state represents the dynamic collision of the rail with the hardened surface of the fouled ballast. These dynamic effects were not covered by the proposed model, but, from observations in the field, they are minimal, and the situation is definitive. However, it is necessary to realize that this final state represents a limiting state since the large, measured displacements during the passage of the train composition do not, in any case, correspond to the safe condition of the track because, in such cases, there is a great risk of derailment.

In a continuation of this research, it would be necessary to confirm some of the presented results by using more complex mathematical models, at least in the initial and final states. The latter state corresponds to the floating sleeper phenomenon. Also, it would be beneficial to indicate other shapes/types of pulse loadings, which may produce higher values of maximal dynamic factor than those analyzed in the current paper. Based on the obtained and new results, advanced recommendations for more appropriate construction and maintenance of railroads, particularly in karst areas, could be provided.

## 5. Conclusions

Dynamic influences have a markedly unfavorable effect on the degradation of rail sleepers and should not be neglected. Based on the results presented in this study, it can be concluded that the complex floating sleeper phenomenon (encountered in Slovenia and many other countries) can be adequately, at least qualitatively, described by a proposed simplified SDOF mathematic model that includes one degree of freedom. Despite its simplicity, it enables the understanding of the key factors influencing the deterioration of the ballast railway track.

The results of the presented research can be summarized as follows:

- A simplified SDOF mathematical model for the quantification of the influences on the floating sleeper phenomenon has been developed.

- For mathematical modeling of the phenomenon, extensive field measurements were carried out, which yielded interesting results, enabled the identification of interesting phenomena and findings, and enabled the simplification of mathematical modeling.
- Based on the actual field measurements and some recommendations from the recent scientific literature, the loading was modeled as a pulse loading of different shapes/types.
- Calculating the maximal dynamic factor reveals that the floating sleeper phenomenon is highly non-linear. The initial response of the sleepers is elastic, but with a reduction in stiffness due to different phenomena, the maximal dynamic factor can significantly increase, which again influences a response in the form of damaged tracks. The final damaged state corresponds to the floating sleeper phenomenon, which aligns with lower values of maximal dynamic factors and relates to the dynamic collision of a rail with the hardened surface of fouled ballast, with a low value for the dynamic factor.

The presented study has detected several issues that should be addressed in future research:

- The accuracy of the applied pulse loadings should be evaluated and compared/discussed with state-of-the-art mathematical models.
- The rate of wear of the ballast and its critical threshold should be identified. Given that this sub-phenomenon is related to dynamic stability—that is, an abrupt change in the ballast's behavior, which relates to approaching the bifurcation point in the accompanying mathematical model—this could be an extremely challenging undertaking.
- As ballast wear contributes significantly to a reduction in track stiffness, the long-term implications of this wear on the safety and performance of railway tracks should be carefully addressed.
- The assumptions of the SDOF model, particularly those that ignore damping and the impact of adjacent structural elements, should be checked.
- In general, additional research (theoretical and experimental) is needed, which will confirm the obtained results and improve the explanation of the entire phenomenon of floating sleepers.

**Author Contributions:** Conceptualization, M.U., I.P. and D.I.; methodology, I.P. and M.U.; software, D.I.; validation, M.U., I.P. and D.I.; formal analysis, I.P. and M.U.; writing—original draft preparation, M.U. and I.P.; writing—review and editing, I.P., M.U. and D.I.; visualization, I.P. and D.I.; project administration, M.U. All authors have read and agreed to the published version of the manuscript.

**Funding:** This research was funded by the Ministry of Infrastructure of the Republic of Slovenia and Slovenian Research Agency (Project: Development of an innovative railway sleeper, V2-1740). The project ended on 31 March 2021.

**Data Availability Statement:** No additional data are publicly available. Interested readers can request/ask for the experimental field measurement data.

**Conflicts of Interest:** The authors declare no conflicts of interest.

## References

1. Ramadan, A.N.; Jing, P.; Zhang, J.; El-Din Zohny, H.N. Numerical Analysis of Additional Stresses in Railway Track Elements due to Subgrade Settlement Using FEM Simulation. *Appl. Sci.* **2021**, *11*, 8501. [[CrossRef](#)]
2. Feng, H. 3D models of Railway Track for Dynamic Analysis. Master's Thesis, Royal Institute of Technology, Stockholm, Sweden, 2011.
3. Winkler, E. *Vorträge über Eisenbahnbau, Heft 1, 2*, Verlag H; Dominicus: Prag, Czech Republic, 1867.
4. Winkler, E. *Die Lehre von der Elasticität und Festigkeit—Mit Besonderer Rücksicht auf ihre Anwendung in der Technik, für Polytechnische Schulen, Bauakademien, Ingenieure, Maschinenbauer, Architekten, etc.*; Verlag H. Dominicus: Prag, Czech Republic, 1867.
5. El Moueddeb, M.; Louf, F.; Boucard, P.A.; Dadie, F.; Saussine, G.; Sorrentino, D. An Efficient Numerical Model to Predict the Mechanical Response of a Railway Track in the Low-Frequency range. *Vibration* **2022**, *5*, 326–343. [[CrossRef](#)]
6. Zhai, W.M.; Sun, X. A detailed model for investigating vertical interaction between railway vehicle and track. *Veh. Syst. Dyn.* **1994**, *23*, 603–615. [[CrossRef](#)]



7. Rodrigues, A.F.S.; Dimitrovova, Z. Applicability of a Three-Layer Model for the Dynamic Analysis of Ballasted Railway Tracks. *Vibration* **2021**, *4*, 151–174. [[CrossRef](#)]
8. Hurtado-Hurtado, G.; Morales-Velazquez, L.; Valtierra-Rodriguez, M.; Otremba, F.; Jáuregui-Correa, J.C. Frequency Analysis of the Railway Track under Loads Caused by the Hunting Phenomenon. *Mathematics* **2022**, *10*, 2286. [[CrossRef](#)]
9. Kurhan, D.; Kurhan, M.; Horváth, B.; Fischer, S. Determining the Deformation Characteristics of Railway Ballast by Mathematical Modeling of Elastic Wave Propagation. *Appl. Mech.* **2023**, *4*, 803–815. [[CrossRef](#)]
10. Yao, S.; Xie, W.; Geng, J.; Xu, X.; Zheng, S. A Numerical Analysis of the Non-Uniform Layered Ground Vibration Caused by a Moving Railway Load Using an Efficient Frequency–Wave-Number Method. *Mathematics* **2024**, *12*, 1750. [[CrossRef](#)]
11. Cai, C.; Tian, S.; Shi, Y.; Chen, Y.; Li, X. Influencing Factors Analysis in Railway Engineering Technological Innovation under Complex and Difficult Areas: A System Dynamics Approach. *Mathematics* **2024**, *12*, 2040. [[CrossRef](#)]
12. Liu, H.; Rahman, M.; Rahimi, M.; Starr, A.; Durazo-Cardenas, I.; Ruiz-Carcel, C.; Ompusunggu, A.; Hall, A.; Anderson, R. An autonomous rail-road amphibious robotic system for railway maintenance using sensor fusion and mobile manipulator. *Comput. Electr. Eng.* **2023**, *110*, 108874. [[CrossRef](#)]
13. Yang, C.; Sun, Y.; Ladubec, C.; Liu, Y. Developing Machine Learning-Based Models for Railway Inspection. *Appl. Sci.* **2021**, *11*, 13. [[CrossRef](#)]
14. Offenbacher, S.; Neuhold, J.; Veit, P.; Landgraf, M. Analyzing Major Track Quality Indices and Introducing a Universally Applicable TQI. *Appl. Sci.* **2020**, *10*, 8490. [[CrossRef](#)]
15. Park, B.; Choi, Y.-T.; Hwang, S.H. Ballasted Track Status Evaluation Based on Apparent Track Stiffness Index. *Appl. Sci.* **2020**, *10*, 4729. [[CrossRef](#)]
16. Uranjek, M.; Štrukelj, A.; Lenart, S.; Peruš, I. Analysis of influential parameters for accelerated degradation of ballast railway track. *Constr. Build. Mater.* **2020**, *261*, 119938. [[CrossRef](#)]
17. Esveld, C. *Modern Railway Track*, 2nd ed.; MRT-Productions: Delft, The Netherlands, 2001.
18. Chopra, A.K. *Dynamics of Structures: Theory and Applications to Earthquake Engineering*; Pearson/Prentice Hall: Old Bridgem, NJ, USA, 2007.
19. Mezeh, R.; Mroueh, H.; Hosseingholian, M.; Sadek, M. New approach for the assessment of train/track/foundation dynamics using in-situ measurements of high-speed train induced vibrations. *Soil Dyn. Earthq. Eng.* **2019**, *116*, 50–59. [[CrossRef](#)]

**Disclaimer/Publisher’s Note:** The statements, opinions and data contained in all publications are solely those of the individual author(s) and contributor(s) and not of MDPI and/or the editor(s). MDPI and/or the editor(s) disclaim responsibility for any injury to people or property resulting from any ideas, methods, instructions or products referred to in the content.